ACADEMIC PRESS

Available online at www.sciencedirect.com

SCIENCE DIRECT®

Icarus 162 (2003) 344–361

ICARUS

www.elsevier.com/locate/icarus

The 10 October 1999 HIP 9369 occultation by the northern polar region of Jupiter: ingress and egress lightcurves analysis

E. Raynaud,[a,*] P. Drossart,[a] K. Matcheva,[a] B. Sicardy,[a] W.B. Hubbard,[b] F. Roques,[a] Th. Widemann,[a] G.R. Gladstone,[c] J.H. Waite,[d] D. Nadeau,[e] P. Bastien,[e] R. Doyon,[e] R. Hill,[b] M.J. Rieke,[f] and M. Marley[g,1]

[a] *LESIA, CNRS-FLE2461, Observatoire de Paris, 5 place Janssen, 92195 Meudon Cedex, France*
[b] *Lunar and Planetary Laboratory, University of Arizona, Tucson, AZ 85721-0092, USA*
[c] *Southwest Research Institute, 6220 Culebra Road, P.O. Drawer 28510, San Antonio, TX 78228-0510, USA*
[d] *Atmospheric, Oceanic, and Space Science Department, University of Michigan, 2455 Hayward, Ann Arbor, MI 48109-2143, USA*
[e] *Observatoire du Mont Mégantic et Département de Physique, Université de Montréal, C.P. 6128, Montréal H3C 3J7, Canada*
[f] *Steward Observatory, University of Arizona, Tucson, AZ 85721-0065, USA*
[g] *Astronomy Department, New Mexico State University, Las Crucas, NM 88003-8001, USA*

Received 12 June 2002; revised 21 November 2002

Abstract

The occultation of bright star HIP9369 by the northern polar region of Jupiter was observed from four locations in North and South America, providing four data sets for ingress and egress. The inversion of the eight occultation lightcurves provides temperature profiles at different latitudes ranging from 55°N to 73.2°N. We estimate the errors on the profiles due to the uncertainties of the inversion method and compare the value of the temperature at the deepest level probed (~ 50 μbar) with previous observations. The shape of the temperature gradient profile is found similar to previous investigations of planetary atmospheres with propagating and breaking gravity waves. We analyze the small scale structures in both lightcurves and temperature profiles using the continuous wavelet transform. The calculated power spectra of localized fluctuations in the temperature profiles show slopes close to -3 for all eight profiles. We also isolate and reconstruct the three-dimensional geometry of a single wave mode with vertical and horizontal wavelengths of respectively 3 and 70 km. The identified wave is consistent with the gravity wave regime, with a horizontal phase speed nearly parallel to the planetary meridian. Nevertheless, the dissipation of the corresponding wave in Jupiter's stratosphere should preclude its detection at the observed levels and an acoustic wave cannot be ruled out.

Keywords: Jupiter; Occultations; Atmospheres, Dynamics; Atmospheres, Structure

1. Introduction

On 10 October 1999, the bright star HIP 9369 (K magnitude 6.5) was occulted by the northern polar region of Jupiter. Whereas previous stellar occultations by Jupiter such as the β Scorpii A and C occultations (Combes et al., 1971; Hubbard et al., 1972) and the SAO 78505 occultation (Hubbard et al., 1995) concerned equatorial and high southern latitudes, the 1999 occultation was the first observed one to sample the northern atmosphere of the planet at high latitudes.

We observed this event from four different locations in South and North America using the facilities of the ESO Very Large Telescope (VLT/ANTU) in Chile[2], the Steward Observatory at Kitt Peak and Catalina Station, both located in Arizona, and the Mégantic Observatory in Québec. Our

* Corresponding author. Fax: +33-145-0771-10.
E-mail address: elisabeth.raynaud@obspm.fr (E. Raynaud).
[1] Currently at NASA-AMES.

[2] Based on observations collected at the European Southern Observatory, Chile (ESO No.64.S-0029(A)).

0019-1035/03/$ – see front matter
doi:10.1016/S0019-1035(03)00005-8

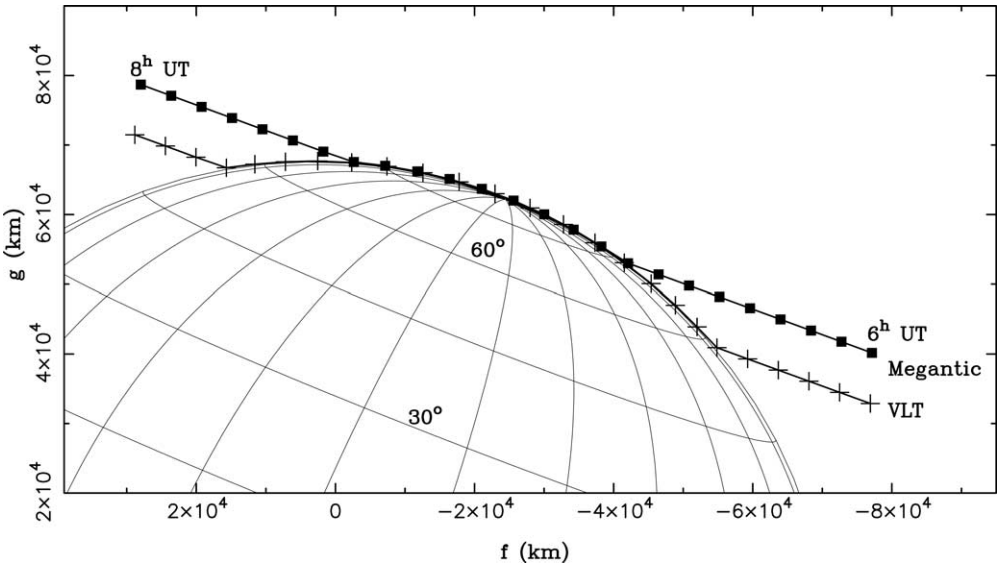

Fig. 1. Geometry of the occultation. The two stellar paths on Jupiter as seen from Mégantic (squares) and the VLT (crosses) are represented. The star paths for Catalina and Kitt Peak would be indistinguishable from the Mégantic one at this scale. The time span between two consecutive symbols is five minutes. The quantities f and g are the coordinates in the sky plane and have their origin at the estimated center of the planet.

objectives are to retrieve temperature profiles from the occultation lightcurves and analyze them for the presence of small and medium scale thermal structures that could contain clues for the local atmospheric dynamics. The four observations probed the atmosphere of Jupiter along different chords, three of them being only a few kilometers apart (Fig. 1). This allows us to compare and correlate these atmospheric structures, to study their coherence in space and time, to determine their spectral characteristics, and even to reconstruct their three-dimensional geometry.

The detection and characterization of small scale temperature fluctuations in the outer planets' atmospheres, as well as the determination of the exact structure of the upper atmosphere, are the key to understanding the processes responsible for thermospheric heating (Young et al., 1997). This is a necessary step in explaining the high thermospheric temperatures of the giant planets, which is one of the most important issues in comparative studies of planetary atmospheres. Studies of small scale structures in the temperature profiles of Jupiter derived from stellar occultations have been attempted before. French and Gierasch (1974) pointed out the presence of sharp spikes in the lightcurves of the β Sco occultation by Jupiter and suggested a possible connection with atmospheric turbulence and propagating waves. Their single temperature profile, however, did not contain direct information on the horizontal structure of the observed wave-like feature and, as a result, the energy carried by the hypothetical wave and its direction of propagation remained speculative. Similar studies have also been performed on other planets, such as Neptune: analysis of the temperature profiles retrieved from the Voyager 2 radio occultation revealed quasi-periodic oscillations in the troposphere and the stratosphere of the planet (Hinson and Magalhaes, 1993). We present here a new study of the temperature structure of the Jovian atmosphere, as well as new techniques of high interest to the reduction of occultation data.

2. Observations

The circumstances of observations for all four sites are given in Table 1. At the Mégantic Observatory, we observed the occultation with the 1-m telescope, using the infrared camera MONICA at 2.2 μm (Nadeau et al., 1994). The timing was controlled by a GPS device and, except for two short discontinuities in the middle of the occultation, due to time calibration of the GPS device, an image was taken every 1.37 s on average, with an integration time of 0.4 s. At 2.2 μm, the limb of Jupiter is very dark, due to strong methane absorption; we are thus able to follow the star along the limb of the planet throughout the whole occultation. Infrared imaging was also used at Kitt Peak (1.6 μm) and Catalina (0.89 μm). A description of the instruments and details of such observations can be found in Hubbard et al. (1995). The short sampling time of these observations, 0.17 and 0.2 s respectively, renders them superior to the rest of the data sets in terms of vertical resolution and makes them very suitable for studies of small scale structures and their spatial spectrum.

The VLT observations were taken with the imaging spectrometer ISAAC (Cuby et al., 2000), in long slit mode, during the occultation between 6:19 and 8:15 UT on 10 October 1999. The 2 arcsec slit was centered on the star, with accurate offset guiding on a guide star; the pointing accuracy and stability was checked after the occultation, to be $\sim$ 0.15 arcsec. One individual frame consists in a 1D image recording the star and eventually the Jupiter limb, and

Table 1
Conditions of observation

Site	Latitude longitude	Telescope diameter (m)	Sampling rate (s)	λ_{obs} (μm)	$\varepsilon\sqrt{\frac{v_\perp}{H}}$
Very Large Telescope (VLT)	24°37′33″S 70°24′11″W	8	1.7	2.31–2.45	0.025 (I) 0.023 (E)
Catalina Station (Cat)	32°25′01″ N 110°43′55″ W	1.54	0.2	0.89	0.009 (I) 0.012 (E)
Steward Observatory Kitt Peak (KP)	31°57′47″ N 111°35′58″W	2.2	0.17	1.6	0.010 (I) 0.023 (E)
Mégantic Observatory (Meg)	45°27′18″ N 71°09′12″W	1	1.37	2.2	0.016 (I) 0.019 (E)

a spectrum recorded between 2.31 and 2.46 μm, at a resolving power of 1200. For both immersion and emersion, the slit was aligned parallel to the Jupiter limb during the observations. The repetition time between two spectral images is 1.7 s, and the integration time is 1 s. The seeing during occultation was lower than 1 arcsec; it has been checked within the occultation data, from the width of a gaussian fit to the 1D star image. Since the seeing varied during the observations, a correction was made to take into account the portion of the star flux falling outside the 2 arcsec slit, but this correction appears to be negligible. The star observations before and after occultation are used as stellar reference, and the observed occulted data are divided by the star spectrum to get the relative occulted data. The full analysis of the VLT spectral occultation will present a complete data description (Drossart et al., in preparation); the data used in this paper correspond to the spectrally co-added lightcurve and can be directly compared to the observations from other sites.

3. Data reduction

For the Catalina and Kitt Peak data, the reduction of images to lightcurves is performed in the same way as described in Hubbard et al. (1995). To remove the background flux from the planet, templates are generated and subtracted from every image. The remaining signal is then integrated in a 6 arcsec aperture centered on the star image.

In the case of the VLT observations, the limb flux is fainter due to the 2.2 μm methane absorption band and we are able to directly separate the stellar flux from the background flux. To do so, we first sum each image in the spectral direction, obtaining a one-dimensional distribution of the intensity versus the position of the pixel on the slit. Assuming that the flux coming from the planetary limb does not vary too much with latitude, we use the intensity curve outside the star area to model the limb intensity near the star image, with a spline approximation. We then extract the star signal as a Gaussian function superimposed on the approximated limb curve and we integrate this function to obtain the total stellar flux. This procedure is performed for each image separately. In addition, the study of the spectral dimension of the data allows us to estimate the atmospheric transmission along the line of sight from the depth variations of the methane absorption bands; we can then correct the lightcurves for methane absorption.

For Mégantic, each image is first summed in the vertical dimension of the mosaic, i.e., along the north–south direction in the sky plane, in order to obtain a one-dimensional intensity profile. This limb intensity curve was then approximated satisfactorily enough by a second degree polynomial. The star flux was then obtained in a similar manner as for the VLT spectra. The resulting lightcurves for all four observations are shown in Fig. 2. For all lightcurves, we calculate a dimensionless measure of the noise $\epsilon\sqrt{v_\perp/H}$ (French *et al.*, 1978), where e is the noise per second of the normalized flux, $v_\perp$ is the star speed perpendicular to the limb, and H is the scale height. The calculated parameters are given in Table 1. We see that the Catalina data for ingress is the best we have. We thus take this observation as a reference for the rest of this work. Catalina egress, Kitt Peak ingress, and both ingress and egress for Mégantic have the same noise level that is low enough for inversion. The Kitt Peak egress curve is much more noisy than the others, and we will be cautious about its analysis in the following sections. The VLT curves also have high dimensionless noise levels, due to the larger $v_\perp$ ($v_\perp \sim 8.2$ km s^{-1} for the VLT, and $v_\perp \sim 4.6$ km s^{-1} for the three other data sets).

4. Isothermal fits

The direct method to derive information from occultation lightcurves is the curve fitting method (see for instance Wasserman and Veverka, 1973). We performed isothermal fits to the lightcurves to estimate the scale height H of the atmosphere and determine the half-light time $t_{1/2}$ for the occultation. Isothermal lightcurves are simulated using the Baum and Code (1953) equation

$$\frac{(z' - z'_0)}{H} = \left(\frac{\phi_1}{\phi} - 2\right) + \log\left(\frac{\phi_1}{\phi} - 1\right), \qquad (1)$$

where z' is the distance of the observer to the center of Jupiter's shadow, z'_0 is this distance at half-light time, ϕ is the stellar flux, and ϕ_1 is the flux of the unocculted star.

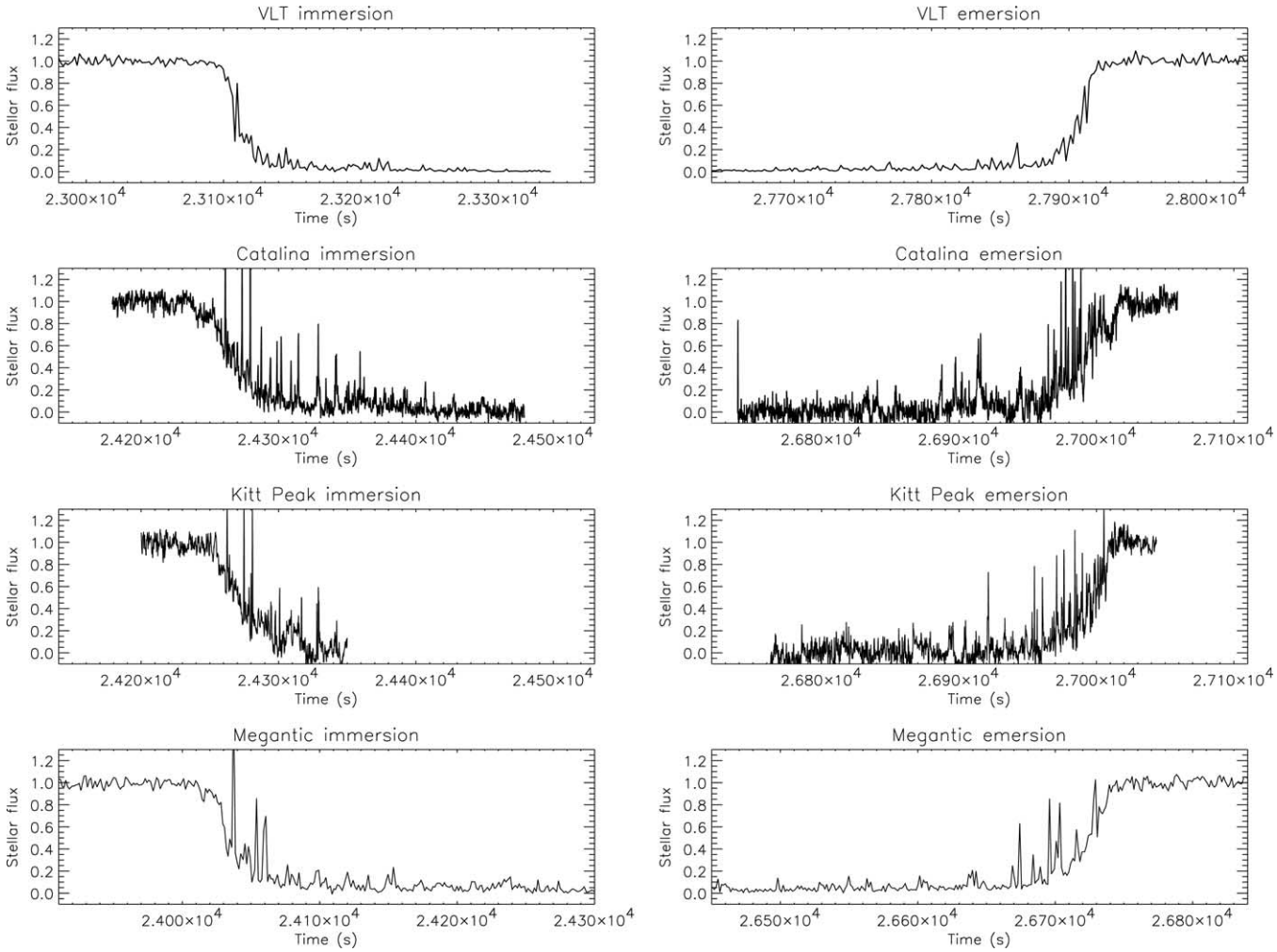

Fig. 2. Ingress and egress occultation lightcurves for all four observations. The unocculted stellar fluxes have been normalized to unity and all four curves have the same time span for ingress and egress.

The free parameters of this model are the scale height H and the half-light time $t_{1/2}$, which determines the position z'_0. The best fits to the observed lightcurves are calculated with a least-square fit routine. The fitting procedure minimizes the residual between model and observations $r = \sqrt{\Sigma_N ((\phi\text{-}\phi_{model})^2/N)}$, where N is the number of points in the data series, ϕ is the observed flux, and ϕ_{model} the isothermal model. The resulting parameters are given in Table 2, along with errors representing a 95% confidence level. Our estimates for the scale height are in good agreement with the values calculated for previous occultations by Jupiter, between 20 and 30 km (Combes et al., 1971; Hubbard et al., 1995). As we pointed out earlier, the previous occultations sampled the atmosphere at very different lati-

Table 2
Parameters of the isothermal fits to the lightcurves

Site	Event	Latitude (deg.)	Longitude (deg. L_{III})	Half-light time $t_{1/2}$ (s UT)	Scale height H (km)	Temperature (K)
Catalina	Ingress	73.13	225.78	24266.4 ± 1.2	28. ± 2.8	195 ± 19.5
	Egress	69.63	93.33	26990.4 ± 1.6	27.6 ± 3.5	192.2 ± 24.4
Kitt Peak	Ingress	73.11	225.84	24270.6 ± 1.2	24.8 ± 2.7	172 ± 18.8
	Egress	69.60	93.39	26997.0 ± 1.1	18.9 ± 1.9	131.6 ± 13.2
Mégantic	Ingress	73.17	223.46	24037.3 ± 1.3	29.7 ± 3.4	206.8 ± 23.7
	Egress	70.26	90.95	26721.4 ± 2.3	29.2 ± 4.1	203.3 ± 28.5
VLT	Ingress	58.14	219.83	23110.0 ± 1.7	23.6 ± 5.8	164.4 ± 40.4
	Egress	55.10	98.36	27909.6 ± 0.9	25.7 ± 2.8	178.9 ± 19.5

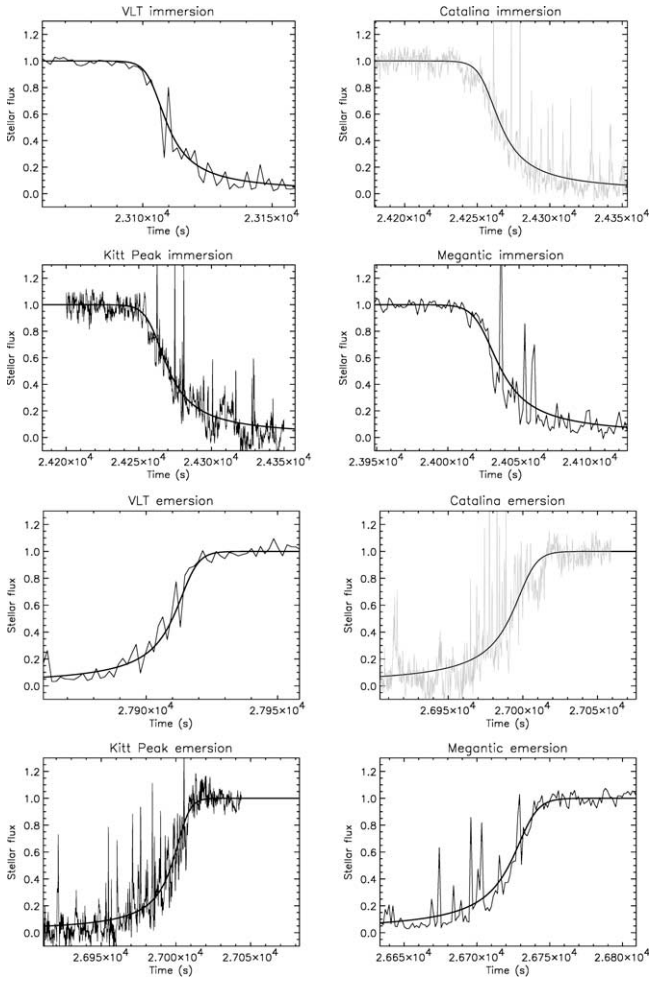

Fig. 3. Isothermal fits performed on the occultation lightcurves (thick smooth curves) are shown superimposed to the data.

tudes and therefore might reflect quite different atmospheric conditions. However, as the Catalina, Kitt Peak, and Mégantic observations probe the same atmospheric region within one degree of latitude, we expect the calculated values for the atmospheric scale height to agree with each other within their respective error bars. And indeed a good agreement is found, with the notable exception of the Kitt Peak emersion value, which seems to be rather low (see Table 2). However, as we saw in Section 3, the Kitt Peak curve is noisier than the others, leading to larger fitting errors on scale heights. The large fitting errors on the scale height in the case of the VLT and the Mégantic observations are mostly due to the sparser time sampling and thus a smaller number of data points.

Fig. 3 shows several large and sharp spikes in the ingress and egress phases that are detectable well above the noise level. The spikes are better defined in the Catalina and Kitt Peak lightcurves, due to a better sampling rate compared to the Mégantic and VLT lightcurves. The observed large spikes reflect significant local departures from the isothermal behavior.

5. Temperature profiles

5.1. The inversion method

We obtain the temperature profiles by inverting the lightcurves with the method given by Vapillon et al. (1973). We perform an Abelian inversion of the lightcurves $\phi(t)$ to obtain refractivity profiles as a function of the radius $\nu(r)$. Assuming that the atmosphere is a perfect gas in hydrostatic equilibrium, we calculate the vertical temperature profile $T_{(z)}$ by integrating the differential equation

$$\frac{dT(z)}{T(z)} = -\frac{dv(z)}{v(z)} - \frac{\overline{\mu(z)}g(z)}{kT(z)}dz, \tag{2}$$

where k is the Boltzman constant, $\bar{\mu}$ is the molecular mass, g is the gravitational field, and z is the altitude above a reference level. The atmosphere of Jupiter is supposed to be composed only of hydrogen and helium. The value of the helium abundance ratio well below the homopause is set to the value measured by the Galileo probe (von Zahn et al., 1998) and a profile of helium abundance in the probed area is generated using a diffusion equation. From the helium abundance profile, we calculate the molecular mass and specific refractivity profiles for the inversion. The parameters adopted for Jupiter's atmosphere are summarized in Table 3.

To have an accurate value of the gravitational field g at each altitude, we calculate the equipotentials of the planet from its gravitational moments and rotational states, and we obtain g as a function of the radius r and the colatitude θ, from the following equations:

$$U(r,\theta) = -\frac{GM}{r}\left[1 - \sum_n J_n\left(\frac{a}{r}\right)^n P_n(\cos\theta)\right] - \frac{1}{2}\omega^2 r^2 \sin^2\theta \tag{3}$$

Table 3
Adopted atmospheric parameters for the inversion

Molecular weight of H_2	2.016 g
Molecular weight of *He*	4.0026 g
Specific refractivity of H_2 at 2.2 μm	5.1111×10^{-30} m^3 molecule^{-1}
Specific refractivity of H_2 at 0.89 μm	5.1290×10^{-30} m^3 molecule^{-1}
Specific refractivity of H_2 at 1.6 μm	5.1129×10^{-30} m^3 molecule^{-1}
Specific refractivity of *He* at 2.2 μm	1.2959×10^{-30} m^3 molecule^{-1}
Specific refractivity of *He* at 0.89 μm	1.2990×10^{-30} m^3 molecule^{-1}
Specific refractivity of *He* at 1.6 μm	1.2964×10^{-30} m^3 molecule^{-1}
Adiabatic index γ	1.423
He abundance ratio at 1 bar	0.1359 ± 0.0027
GM	1.267×10^{17} m^3 s^{-2}
J_2	14697×10^{-6}
J_4	-584×10^{-6}
J_6	31×10^{-6}
a (at 1 bar)	71492 km
Polar radius (at 1 bar)	66848 km

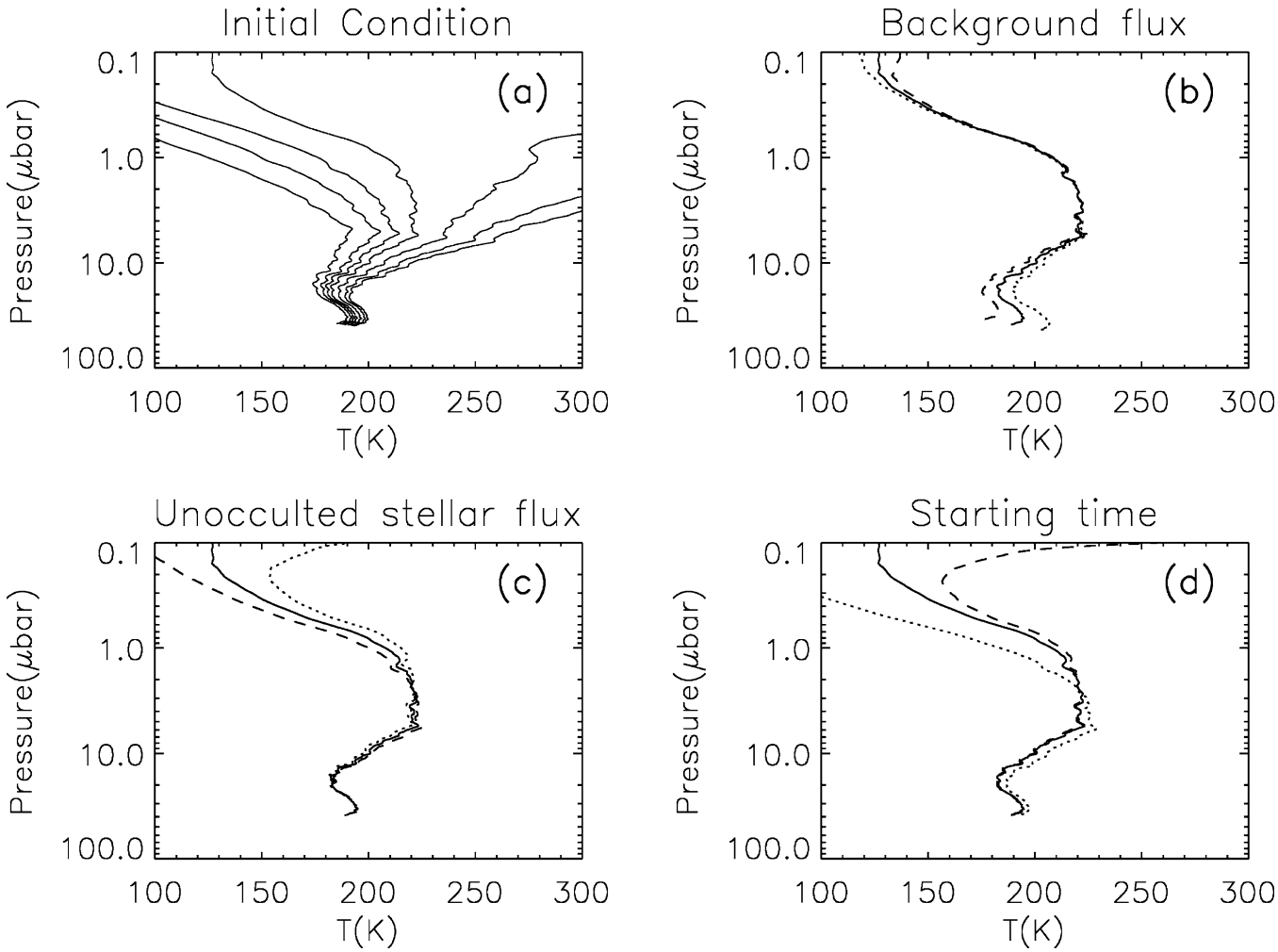

Fig. 4. Influence of some parameters on the inverted temperature profile. The Catalina immersion profile is taken as an example. (a) Temperature profiles obtained for various values of the initial condition of temperature at half-light level: 150, 180, 200, 250, 280, and 300 K. (b) Influence of a variation of 0.01 in the background flux. The dotted line corresponds to an increase and the dashed line to a decrease in the background flux. (c) Influence of a 1% variation in the full stellar flux, with the same plotting symbols as in (b). (d) Inverted profiles obtained for inversion starting times of 24224 s (dotted line), 24230 s (solid line), and 24236 s (dashed line).

$$\vec{g} = -\vec{\nabla}U, \tag{4}$$

where P_n is a Legendre polynomial, J_n are the gravitational moments of the planet, G is the gravitation constant, M is the mass of Jupiter, and a is the equatorial radius.

This inversion method has some well-known drawbacks. The atmospheric refractivity is very small at high altitudes, and the atmospheric signature in the data is overwhelmed by noise. As a consequence, reliable temperature retrievals two scale heights above the half-light level are not possible (Wasserman and Veverka, 1973). From Eq. (2), it is clear that the inversion method requires the temperature to be specified at a given altitude. But no in situ data are available at these latitudes, and this choice is somewhat arbitrary. We choose the half-light level, which corresponds to a pressure of about 1.8 μbar, to impose this initial condition. Different initial conditions lead to very different profiles at high altitudes (Fig. 4), but all of them converge to a stable solution below the half-light level. We fix the temperature initial condition so that the inverted profile remains as stable as possible. It is important to point out that although the large scale structure of the temperature profile can be very sensitive to the initial choice of the temperature, the small scale structure is very robust, i.e., the scales and amplitudes of the small scale temperature fluctuations remain constant even in regions where the absolute value of the temperature shows large variations.

To a lesser extent the retrieved temperature profile is sensitive to the estimation of the background flux, the unocculted stellar flux, or even the choice of the inversion starting time (Roques et al., 1994). In Fig. 4, we show that a small variation (1% of the unocculted stellar flux) in the background flux changes the bottom temperature by more than 10 K and that small variations in the chosen starting time and in the unocculted stellar flux induce changes in the

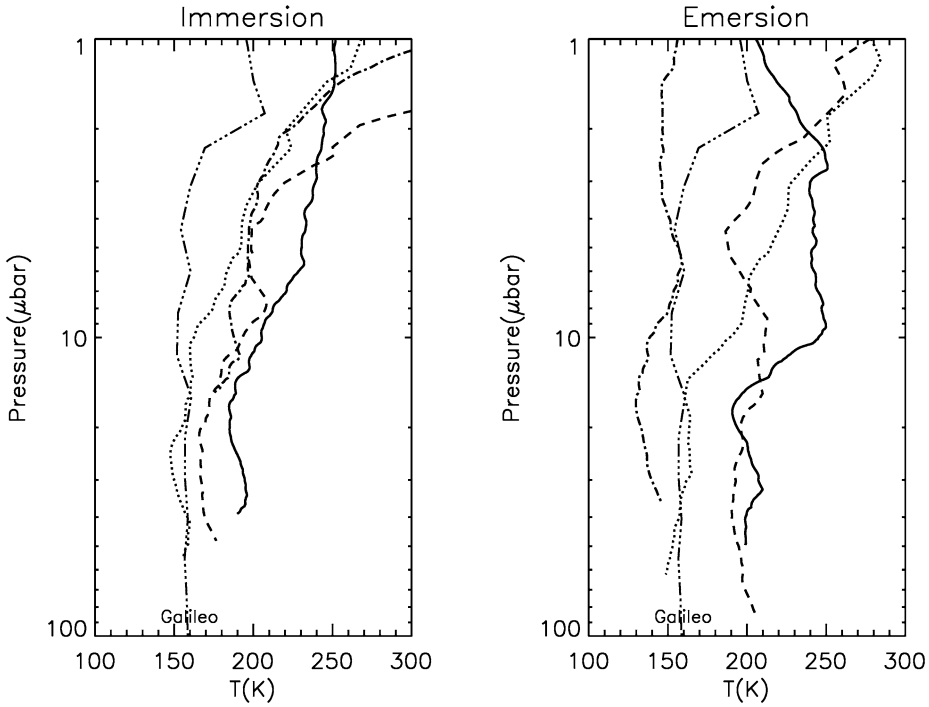

Fig. 5. Temperature profiles as a function of pressure, obtained by inversion of the ingress (left) and egress (right) occultation lightcurves. For both panels, Catalina is a solid line, Kitt Peak a dash-dotted line, Mégantic a dashed line, and the VLT a dotted line. The Galileo profile (Seiff et al., 1996) is displayed for comparison as a dot-dot-dot-dashed line

shape of the profile. If we add up the effects of these parameters, leaving aside the unocculted stellar flux which only influences the top part of the profile, we find that the uncertainty on the absolute value of temperature is on the order of ± 20 K at the bottom of the profile. Finally, we test the influence of methane absorption. For different values of K_{eddy}, we calculate methane abundance profiles and correct the VLT ingress lightcurve for methane absorption. We then invert these corrected lightcurves. The bottom temperature obtained for the average value of $K_{eddy} = 2 \times 10^6$ cm^2 s^{-1} (Drossart et al., 2000) is 10 K warmer than for the uncorrected profile, but once again, the characteristics of the small scale variations, which are of specific interest to this work, remain insensitive to the choice of parameter values even in regions of large temperature uncertainties. In addition, we conclude that the retrieved temperature profiles are quite reliable in the region below the 2 μbar pressure level, within a confidence interval of ± 20 K.

5.2. Profiles

The inverted temperature profiles, both for ingress and egress, are shown in Fig. 5, along with the Galileo temperature profile (Seiff et al., 1996). As foreseen in Section 4, the profiles are not isothermal; they show small scale fluctuations that are particularly noticeable on the Kitt Peak and Catalina profiles, due to their good vertical resolution. However, the absolute values of temperature retrieved by inversion are in good agreement with the results of the isothermal fits, given in Table 2. All the profiles also exhibit quite strong temperature gradients, above the 20 μbar pressure level. For immersion, the four observations result in rather similar profiles. The differences between the three North American observations, which sounded the same atmospheric layer at a latitude of 73° N, are within the uncertainties of the inversion method mentioned in Section 5.1, and the VLT profile (58° N) is a little colder than the other three. We do not find this similarity in the emersion profiles: the Kitt Peak profile is much colder and very different from the Catalina profile, despite the fact that the two observations sounded the same atmospheric layer nearly simultaneously; however, we pointed out in Section 3 that the Kitt Peak emersion profile was hindered by noise problems. Apart from the Kitt Peak case, the profiles show the same behavior as for immersion, i.e., the Mégantic and Catalina profiles are rather close, at least for the bottom part, whereas the VLT profile is colder.

Despite the rather poor sampling of Mégantic and VLT data, we believe this difference to be real. The comparison with the Galileo profile (Seiff et al., 1996) shows that the temperature below the 10 μbar pressure level does not change very much between the equator and the latitudes of the VLT observation (55–58° N), but increases noticeably at high latitudes, of about 40–50 K ($\pm$ 20 K due to the inversion method) at latitudes of 70–74°N. This result is consistent with the work of Grodent et al. (2001), as their

self-consistent model of the thermal structure of the Jovian auroral region finds warmer temperatures in the polar region than the equatorial Galileo profile.

The variations in the temperature profiles at pressures below the 1 mbar pressure level have a pronounced influence on the CH_4 emission in the ν_4 fundamental band at 7.8 μm. Local variations of CH_4 emission, as observed from ground-based observations at 7.8 μm (Orton et al., 1991), are interpreted as oscillations with amplitudes as high as 10 K in the 1–50 mbar range. We test the consistency of our retrieved thermal profiles, in terms of the CH_4 emission, by comparing synthetic spectra calculated with the Galileo probe thermal profile and with the occultation retrieval. Comparison of the CH_4 emission variation between Galileo and the occultation profiles in line by line calculations performed over the 7.8 μm band shows variations lower than 10% in the emission, which are within the range of observed variations. Therefore, we can conclude that our retrieved profiles are consistent with the usual CH_4 observations at 7.8 μm, without invoking peculiar atmospheric conditions in the occultation zone. From now on we will focus on the study of the non-isothermal small scale structures, both in the temperature profiles and in the occultation lightcurves.

6. Lightcurves analysis

6.1. Lightcurve comparison

As alluded to in Section 4, the spikes in the occultation lightcurves correspond to non-isothermal features. We compare these spikes from one curve to another to explore the spatial extent of these features. To be able to compare the lightcurves, we must shift them in time so that the same pressure level is probed at the same time for all four curves. We take Catalina half-light time as a reference time, and we calculate for each of the three other curves an *astrometric half-light time*, i.e., the time at which the star probes the same equipotential surface (see Eqs. (3) and (4)) as is probed at the reference time on the Catalina star path (French et al., 1982). We then shift the other lightcurves so that the astrometric half-light times match the chosen reference time (Fig. 6). We define the *reference point* as the position of the star at the reference time on Catalina stellar path. The VLT stellar chord is 20 degrees south of the three others (Fig. 1) and the planet has also rotated between the VLT occultation and the Catalina one, by 11 degrees for ingress and 9.7 degrees for egress. The distance between VLT half-light point and the Catalina reference point is thus more than 15,000 km. Moreover, no special features can be seen on the VLT immersion lightcurve (Fig. 6), apart from a large peak at the beginning of ingress. Consequently, we choose to look for correlations only between the three North American curves.

Despite the difference in sampling between the curves, we can see in Fig. 6 that some large spikes seem to be correlated between the immersion lightcurves from Catalina, Kitt Peak, and Mégantic: in particular, the three large peaks occurring at $t = -5.5$ s, $t = 6.7$ s, and $t = 12.7$ s after the reference time in the Catalina curve are very similar to the ones in the Kitt Peak curve ($t = -8.33$ s, $t = 3.90$ s, and $t = 10.02$ s) and the ones in the Mégantic curve ($t = -1.32$ s, $t = 15.40$ s, and $t = 22.13$ s). We refer to these peaks as peaks A, B, and C as indicated in Fig. 6. We calculate the time delay between each Catalina peak and the corresponding ones in Kitt Peak and Mégantic lightcurves; we find that these time delays are the same between Catalina and Kitt Peak for peaks A, B, and C ($\Delta t = 2.8 \pm 0.1$ s) as well as between Catalina and Mégantic for peaks B and C ($\Delta t = -9.1 \pm 0.4$ s). These peaks could thus be the signatures of the same kind of non-isothermal features for all star paths. In Fig. 7, we plot the star paths for Catalina, Kitt Peak, and Mégantic in a three-dimensional local frame in Jupiter's atmosphere, along with the locations of peaks A, B, and C for each observation. These locations were determined by the positions of the star's image on the stellar paths at the times of peaks A, B, and C for a model isothermal atmosphere of scale height $H = 25$ km. The results we present here and in Section 8 are not significantly modified for an isothermal atmosphere of scale height $H = 30$ km. We find that the three points for each peak are located in nearly parallel planes, that we accordingly name planes A, B, and C. This three-peak structure is clearly a signature of peculiar atmospheric behavior that will be studied in Section 8. To search for other groups of peaks of the same shape, scale and time delays between the different lightcurves, we perform a scale-time analysis of the lightcurves, using the continuous wavelet transform (CWT) (Farge, 1992).

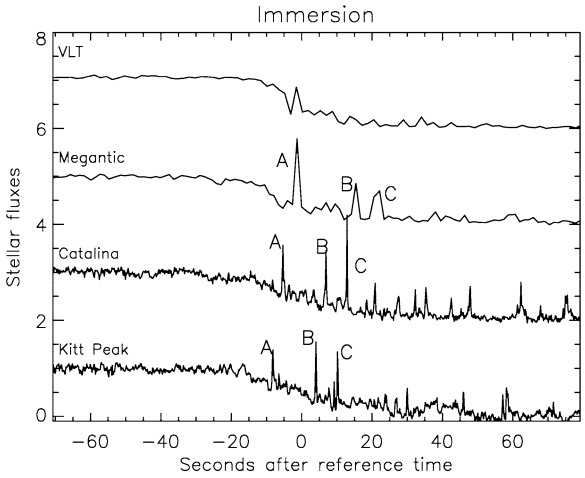

Fig. 6. Immersion lightcurves displayed in a common time scale. The reference time is the Catalina half-light time. The three other curves have been shifted in time to match their astrometric half-light times with the reference time. Constants equal to 2,4, and 6 respectively for Catalina, Mégantic, and the VLT have been added to the stellar fluxes for better display. Peaks A, B, and C are labeled for each curve (see text).

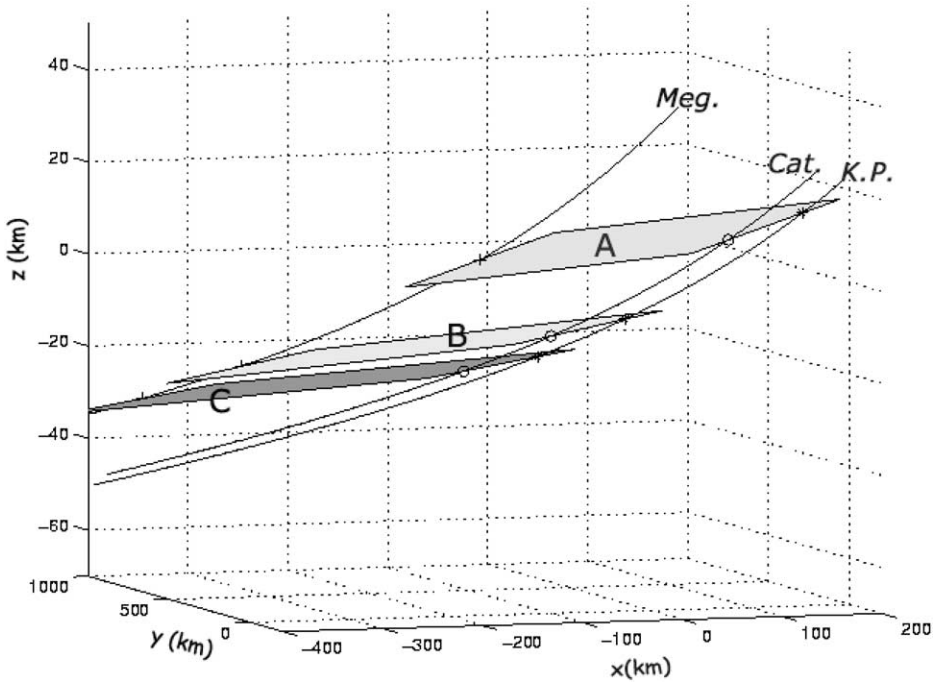

Fig. 7. Positions of planes A, B, and C in Jupiter's atmosphere. On the plot, we show a limited region of the atmosphere around the reference points. The *x* and *y* coordinates are the distances from the reference point, respectively, along a parallel and a meridian of Jupiter, perpendicularly to the *z* axis. *x* increases in the direction of the equator (southward), and *y* increases eastward. The *z* coordinate is the altitude above the reference point, in a topographic frame (i.e., the *z* axis is perpendicular to the equipotentials). The lines labeled Meg., Cat., and K.P. are the three stellar paths for Mégantic, Catalina, and Kitt Peak, respectively. Planes A, B, and C, formed by the peaks A, B, and C on each path, are shown in different shades of gray (see text).

6.2. Wavelet analysis

Wavelet analysis is a powerful tool to analyze localized variations of intensity in a time series. It allows the decomposition of a signal into a time-frequency space, so that modes of variability as well as their changes in time are identified. A regularly sampled data series is decomposed on a set of functions which are scaled and translated versions of a single function ψ_0 called the *wavelet function* or *mother function.* The mother function needs to have zero mean, to be localized in both time and scale spaces, and to be normalized to have unit energy. A review of the admissible mother functions and their properties can be found in Farge (1992). The choice of the mother function does not drastically change the qualitative results of the wavelet decomposition; however, Torrence and Compo (1998) show that real mother functions are more efficient in detecting sharp irregularities in a signal, while complex mother functions should be used to reveal oscillatory behaviors in the analyzed data. Perrier et al. (1995) also point out that the wavelet power spectrum, which we calculate later in this work, is meaningful only if the mother function has enough vanishing moments. That is why we choose to use the sixth derivative of a gaussian (Eq. (5)), referred to as DOG6, for the wavelet analysis of the lightcurves. We will use the Paul wavelet function of parameter 4 (Eq. (6)) for the analysis of the temperature fluctuations in Section 7.

$$\psi_0^{DOG}(x) = \frac{-1}{\sqrt{\Gamma\left(\frac{13}{2}\right)}} \frac{d^6}{dx^6} (\exp - x^2/2) \tag{5}$$

$$\psi_0^{Paul}(x) = \frac{2^4 \cdot 4!}{\sqrt{\pi 8!}} (1 - ix)^{-5} \tag{6}$$

The CWT (see Torrence and Compo, 1998) of a time series (ϕ_n) is defined by

$$W_n(s) = \sum_{n'=0}^{N-1} \phi_{n'} \psi^* \left[\frac{(n' - n)\delta t}{s} \right], \tag{7}$$

where δt is the time sampling of the data series, s is the *wavelet scale*, and ψ^* is the complex conjugate of the normalized mother function. In the case of the lightcurves, s is a time scale, expressed in seconds. The CWT allows us to construct a two-dimensional map of the signal giving the energy contained in each scale as a function of time (Fig. 8), for a continuous range of scales between the time sampling rate of the data and roughly half the length of the time series. The time resolution of the map is determined by the sampling rate of the original time series. A horizontal cut in the map in Fig. 8 gives the filtered signal for a given scale, and a vertical cut gives the energy repartition between the different scales for a given time.

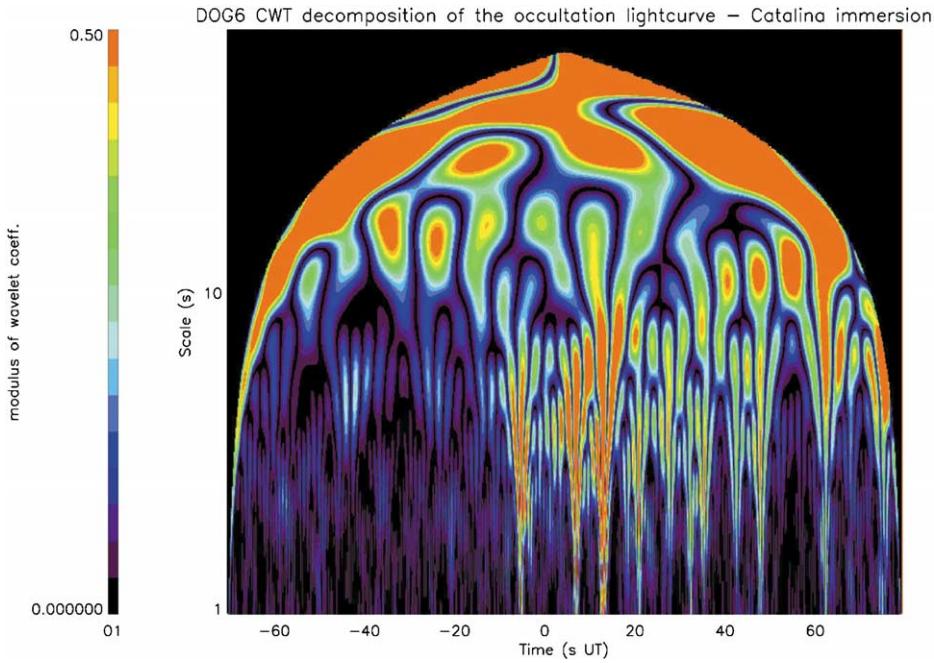

Fig. 8. Wavelet decomposition map of the Catalina ingress lightcurve. The abscissa is the time, in the same units as in Fig. 6, and the ordinate is the wavelet scale. The colors represent the value of the wavelet coefficients of the decomposition, i.e., the energy densities for each point of the time, scale plane. The points affected by edge effects, defining a *cone of influence* depending on the scale, have been removed and appear in black on the map. A cut-off value of 0.5 for the amplitude of the wavelet coefficient had to be introduced, for better reading of the color scale. The three red vertical patches around the reference time correspond to peaks A, B, and C.

We perform a CWT decomposition of the lightcurves from Mégantic, Catalina, and Kitt Peak. By taking a horizontal cut for the smallest scale of the decomposition in the three maps, we can compare the signals of highest frequency ϕ_{Cat}, ϕ_{Kit}, and ϕ_{Meg} by pairs. We introduce between the two filtered signals an artificial shift Δt and calculate the corresponding cross-correlation coefficient

$$CC(\Delta t) = \frac{\sum_{i=1}^{N}(\phi_{Cat}(t_i) - \overline{\phi_{Cat}}) \times (\phi_{Kit}(t_i - \Delta t) - \overline{\phi_{Kit}})}{\sqrt{\sum_{i=1}^{N}(\phi_{Cat}(t_i) - \overline{\phi_{Cat}})^2 \times \sum_{i=1}^{N}(\phi_{Kit}(t_i - \Delta t) - \overline{\phi_{Kit}})^2}} \quad (8)$$

in the case of Catalina and Kitt Peak curves. The quantity $\overline{\phi}$ is the mean value of the correlated function ϕ_1 and N is the number of points $\phi(t_n)$, $n \in \{1, N\}$ in the data series. The local maxima of the cross-correlation function $CC(\Delta t)$ give the time delays yielding the best correlations between the filtered lightcurves. In Fig. 9, we plot the high-frequency filtered lightcurves for Catalina and Kitt Peak, with the Kitt Peak curve shifted in time by $\Delta t = +2.8$ s, corresponding to the best shift. We see that peaks A, B, and C are correlated and that there might be a fourth correlated peak as well (labeled D on Fig. 9), occuring at $t = 30$ s after the reference time. Because of poorer time sampling of the Mégantic data set, the correlation between Mégantic and Catalina filtered lightcurves is not good enough to reveal peak D in the Mégantic curve. Apart from this group of three to four peaks, we could not find any other good correspondence between the wavelet-filtered immersion lightcurves. We can note that in Fig. 9 the number of peaks is not the same in the two data sets and that most of them are not correlated at all. For the emersion lightcurves, we can identify a group of correlated peaks between Kitt Peak and Catalina decomposition, for a shift of $\Delta t = +1.8$ s (shown in Fig. 9), but no correlation at all between Catalina and Mégantic. This can be explained again by the poorer sampling of the Mégantic lightcurve, which does not allow a peak to peak comparison of the data as for Catalina and Kitt Peak. The wavelet analysis allowed us to reveal groups of correlated peaks between two data sets that could not be seen by eye. With only two points for each peak, we can not define a plane such as the planes A, B, and C, but the method has proved to be powerful for correlating sufficiently well sampled data.

7. Temperature fluctuations and power spectra

Up to this point, our study of the observed peaks in the occultation lightcurves has been independent from assumptions and free of arbitrary choices. To further understand the nature of the corresponding atmospheric structures and their implications for the atmospheric state and dynamics, we shall analyze the inverted temperature profiles for the pres-

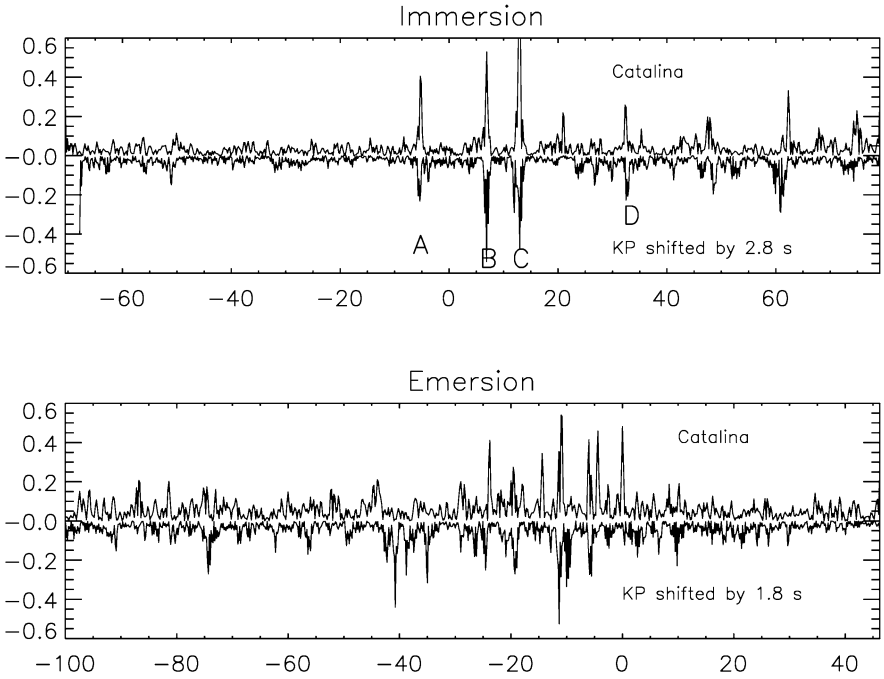

Fig. 9. Filtered lightcurves at highest frequency for Catalina and Kitt Peak. (Upper panel) For ingress, a shift of $\Delta t = 2.8$ s has been imposed on the Kitt Peak curve, represented upside down for better viewing. Peaks A, B, C, and D are shown on both signals (see text). (Lower panel) For egress, the Kitt Peak curve has been shifted by $\Delta t = 1.8$ s.

ence of small and medium scale variations. In Section 5, we showed that the temperature profiles were very dependent on the values of the inversion parameters. However, as we can see in Fig. 5, the inversion parameters change the global shape of these profiles, but do not influence their small scale structure. The temperature gradient and the small scale temperature fluctuations are then much less dependent than the temperature on the values we choose for these parameters.

The temperature gradient profiles for the ingress lightcurves are compared in Fig. 10. For reference, we also plot the adiabatic gradient of Jupiter,

$$\left(\frac{\partial T}{\partial z}\right)_{ad} = -\Gamma = -\frac{g}{c_p}, \tag{9}$$

where $c_p = 1.432 \times 10^4$ J kg^{-1}K^{-1} is the specific heat at constant pressure. The resulting value for the adiabatic lapse rate is $\Gamma = 1.83$ K km^{-1}, for a value of $g = 26.2$ m s^{-2} at the immersion latitude. From now on, all the profiles will be given as functions of altitude z instead of pressure, expressed in kilometers above the half-light level. The half-light level corresponds to a pressure of $\sim$1.8 μbar, yielding an altitude of $\sim$ 300 km above the 1 bar level in comparison with the Galileo profile.

The $\partial T/\partial z$ profiles for all observations exhibit similar features. Small scale quasi-periodic structures can be seen throughout the sampled region. The noticeable difference in the vertical scale of the observed structures in the top and in the bottom part cannot be explained by the decrease of vertical resolution with altitude only; as a matter of fact, the vertical resolution is always better than 1.5 km, and the vertical scale of the observed structures in the upper part of the profile is larger than 10 km (see Fig. 10). Smaller vertical scale structures seem to vanish in the upper atmosphere. The small scale oscillations of the profiles are highly asymmetric with sharp positive peaks and rounded negative excursions. This asymmetry could be enhanced by ray crossing effects at the bottom of the inverted profiles (Sicardy et al., 1999). In any case, we must point out that the atmosphere is stable or marginally stable throughout the region of interest, as the negative values of the temperature gradient never exceed the adiabatic lapse rate.

These gradient profiles are very similar to vertical temperature gradient profiles obtained for stellar or radio occultations on other planetary bodies, such as Titan (Sicardy et al., 1999), Venus (Hinson and Jenkins, 1995), or Neptune (Roques et al., 1994). Most of these profiles were interpreted as signatures for propagating waves saturating whenever the temperature gradient reached the adiabatic lapse rate.

After resampling the profiles at a regular vertical step fixed at $\Delta z = 0.1$ km, we calculate the temperature fluctuations from mean:

$$\epsilon(z_k) = \frac{T(z_k) - \overline{T(z_k)}}{\overline{T(z_k)}}, \tag{10}$$

where z_k, $k \in [1, N]$ are the altitudes of the data points and $\overline{T}$ is a mean temperature profile. This mean profile is reconstructed from a wavelet decomposition of the temperature

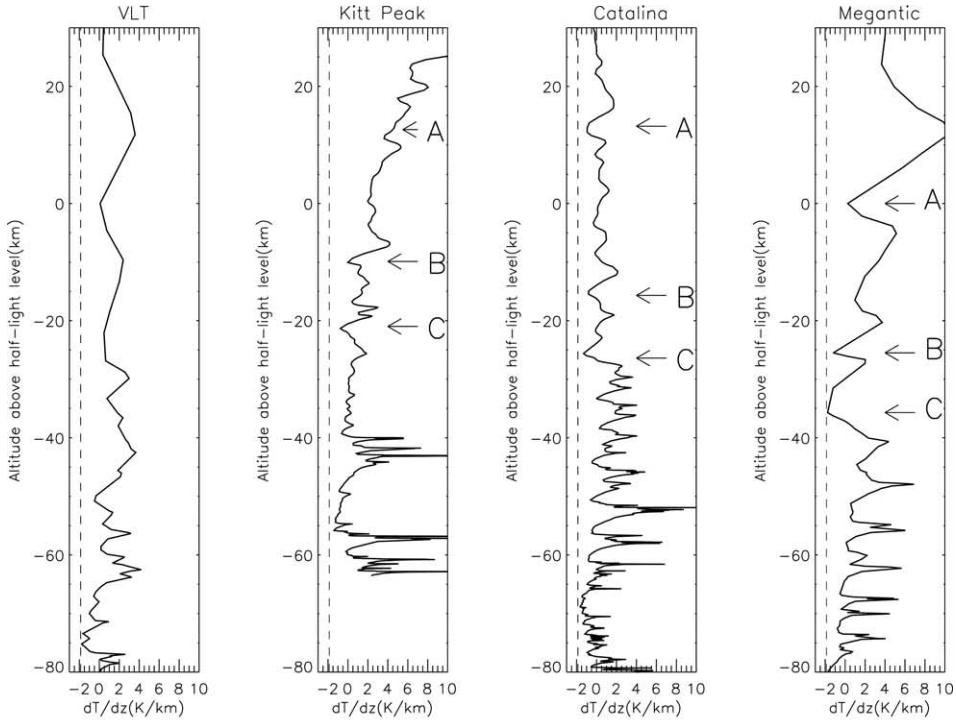

(a) Ingress

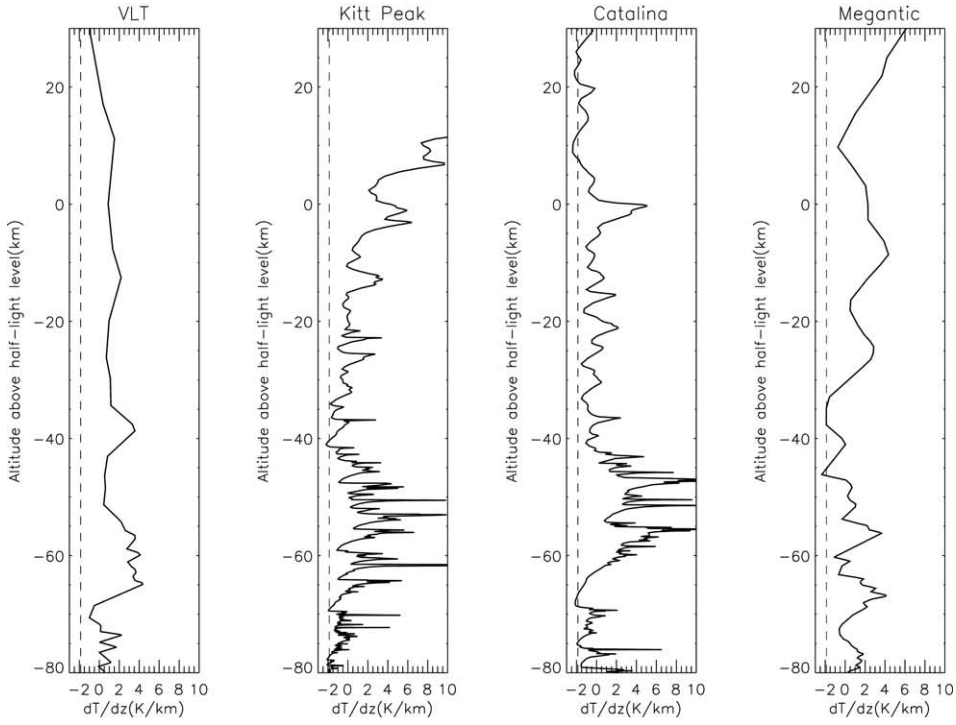

(b) Egress

Fig. 10. (a)Temperature gradient profiles for ingress. The altitudes corresponding to peaks A, B, and C on the lightcurves are indicated by horizontal arrows. On each plot, the adiabatic gradient $(\partial T/\partial z)_{ad} = -\Gamma = -1.83\,\mathrm{K\,km^{-1}}$ is shown for comparison (dotted line) (b) Same as (a), but for egress.

profile retaining only scales larger than a chosen averaging scale s_{mean}. As explained in Section 6, we will from now on use the Paul 4 wavelet (Eq. (6)) to analyze the temperature profiles. For this mother function, the vertical wavelength λ_z of the structures in the CWT decomposition is obtained from the wavelet scale s, by the equation $\lambda_z = (4\pi/9) \times s$. We choose $s_{mean} = 60$ km, corresponding to $\lambda_{z,mean} = 84$ km, as a good compromise between the total height (~250 km) of the probed atmospheric region and the small and medium scale structures that we are studying. According to the results of Section 5, we analyze the temperature profiles only for pressures larger than 0.1 μbar.

We use two different methods to derive the spectrum of the present temperature fluctuations and compare the results for consistency and numerical artifacts. First we perform a Fourier analysis of the temperature fluctuations using the discrete Fourier transform. To avoid windowing effects we multiply the $\epsilon(z)$ profile by a Hann window before calculating the power spectra $|\tilde{\epsilon}(\lambda_z)|^2$ with

$$\tilde{\epsilon}(\lambda_z) = \frac{1}{N}\sum_{k=1}^{N} \epsilon(z_k) \times \frac{1}{2}\left(1 - \cos\left[2\pi\frac{z_k - z_{\min}}{z_{\max} - z_{\min}}\right]\right) \cdot e^{2\pi i z_k/\lambda_z}.$$

The power spectra can also be calculated using a wavelet decomposition, through the CWT described in Section 6. The CWT power spectra is obtained by

$$\overline{W}^2(s) = \frac{1}{N}\sum_{k=1}^{N}|W_k(s)|^2 \qquad (11)$$

with the same notations as above (Torrence and Compo, 1998). We compare the power spectra of the fluctuations in the Catalina ingress temperature profiles, obtained by these two methods (Fig. 11). As expected there is an overall agreement between the two spectra. We can see that the CWT method does not find all the dips introduced by the Fourier transform method that we believe to be numerical artefacts. We performed other tests on the CWT power spectrum calculation: we constructed temperature profiles with a prescribed fluctuation spectrum $P(m_z) \propto m_z^{\alpha}$, where m_z is the vertical wavenumber and α is referred to as the *slope* of the spectrum. We generated synthetic lightcurves from these profiles and processed them through the inversion and power spectrum calculation routines to check if we retrieved properly the prescribed initial spectrum. Our results are satisfactory and consistent with those of Sicardy et al. (1999) performed with a Fourier transform calculation and as in Fig. 11, the wavelet spectra are smoother than the Fourier spectra. The CWT seems then to be a reliable method to calculate the power spectra of temperature fluctuations and its advantage over the Fourier transform calculation is that no calculation artefact on the spectra is generated by this method.

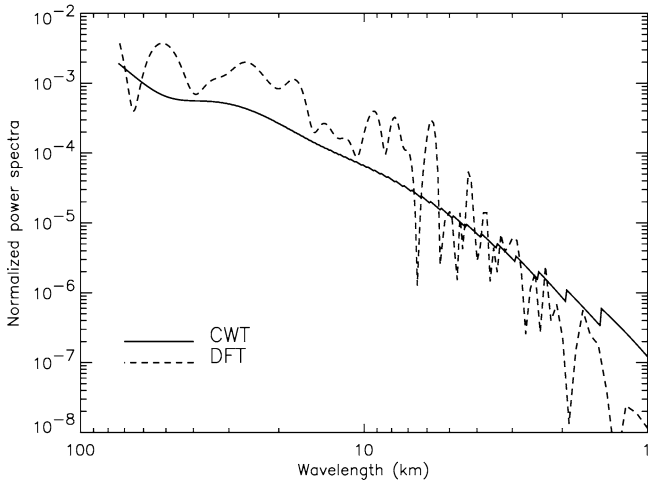

Fig. 11. Comparison of the power spectra of temperature fluctuations, calculated by continuous wavelet transform (full line) and discrete Fourier transform (dashed line).

Using the CWT method, we calculate the power spectra of temperature fluctuations for each ingress and egress profile. In Fig. 12 we plot the mean power spectra, along with the standard deviation, for ingress and egress, calculated by averaging the spectra of the four stations. The vertical wavelength is limited by both the star diameter and the Fresnel scale $\sqrt{\lambda_{obs} D_{Jup-Earth}}$. For our observations, the Fresnel scale ranges from 0.8 to 1.15 km depending on the wavelength of observation λ_{obs} (see Table 1), and the star diameter is of the same order (~1 km). That is why we plot the spectra only for wavelengths larger than 1 km in Fig. 12. The upper wavelength limit is given by $\lambda_{z,mean}$. To estimate the noise level, we calculate the power spectra of temperature fluctuations for an isothermal synthetic lightcurve with a superimposed noise, calculated from the scintillation noise level of the unocculted star. It is easy to see that the detected small and medium scale structures in the temperature profiles are well above the noise level and that the standard deviation around the mean profile is rather small, which indicates a robust power law behavior. The slope of the so-obtained spectrum is close to -3, especially for wavelengths larger than 5 km.

The CWT decomposition allows us to calculate localized spectra of the temperature fluctuations without any loss of information. For this, we divide the temperature profile into 5 km thick layers and calculate the power spectra of the temperature fluctuations within these layers (see Fig. 13). We see that the power spectrum is flatter for the upper part of the profile: the slope of the spectrum is close to -4 at the lowest altitude on Fig. 13, close to -3 at altitudes $z = -46$ km and $z = -21$ km, and flattens even more for the altitudes close to the half-light level ($\alpha \sim -2.3$ at $z = 4$ km). The steeper slope for lower altitudes can be explained by ray crossing effects: Sicardy et al. (1999) showed that ray crossing steepens the slope of the fluctuations' power spectrum, changing a original -3 slope into a -4 slope. In conclusion

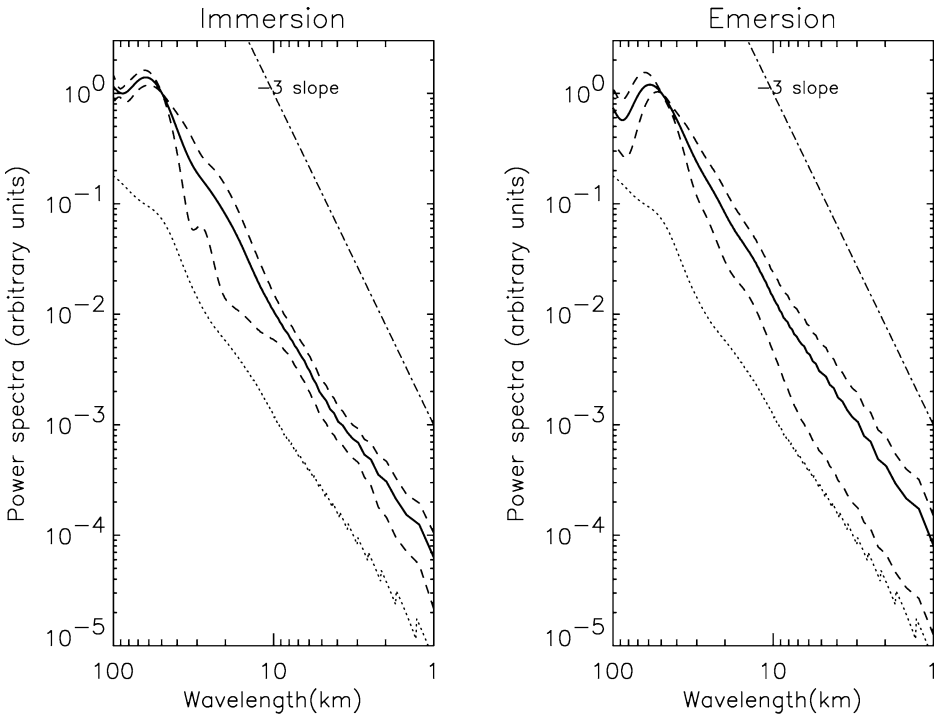

Fig. 12. Power spectra of the temperature fluctuations as a function of the wavelet scale, for immersion and emersion. The mean of the four calculated power spectra is shown as a plain line, along with the standard deviations of this mean (dashed line). The power spectra of an isothermal curve with superimposed noise is displayed as a dotted line (see text). For comparison, we also plot a straight line of slope −3.

of this spectral study, we can say that the global spectrum of the fluctuations in the retrieved temperature profiles has a slope of −3, created essentially by structures in the lower part of the profile (below half-light level). These −3 slope spectra are similar to the so-called *universal −3 spectrum* that has been extensively observed in the Earth's atmosphere (Smith et al., 1987) as well as in other planetary atmospheres (Sicardy et al., 1999). The −3 spectral index is empirically related to the presence of propagating gravity waves in a stratified atmosphere, although the underlying mechanisms for this spectral behavior are not clearly understood yet. It is consistent with the presence of gravity waves with a broad spectrum of wavelengths in the probed atmospheric layers. As gravity waves have already been detected in Jupiter's atmosphere at different latitudes (French and Gierasch, 1974; Young et al., 1997), we now check if the features we detected in the lightcurves (in Section 6) could be caused by propagating gravity waves.

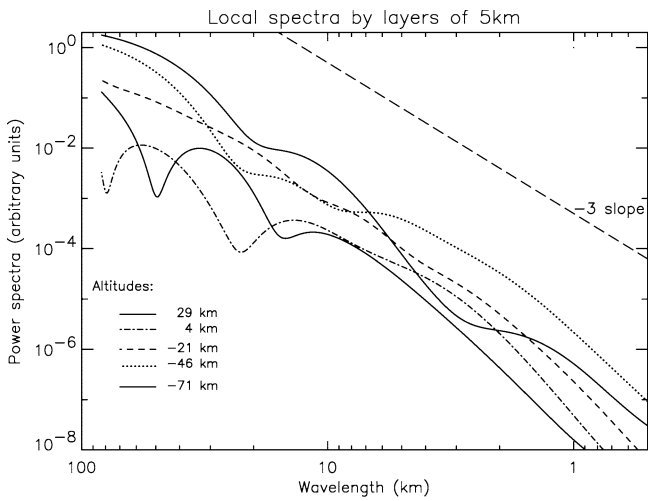

Fig. 13. Power spectrum of temperature fluctuations for five of the 5 km thick layers described in the text. The labels correspond to the central altitude of each layer. A −3 slope is shown for comparison.

8. Wave interpretation

In this section we present possible explanations of the observed small scale structures in the occultation lightcurves and in the derived temperature profiles. In a single event observation like a star occultation, it is impossible to distinguish transient from static features in the atmosphere and as a result, there is an inherent ambiguity in the interpretation of the observed atmospheric structures. We focus on the three-peak system that we identify in the lightcurves from Catalina, Kitt Peak, and Mégantic. The three nearly simultaneous observations allow us to determine the three-dimensional geometry of the observed atmospheric feature. In Section 6 we showed that the locations of the three peaks define a system of three nearly parallel planes. If we interpret the observed peaks as the signature of an atmospheric

wave, these planes correspond to a system of phase planes of the same wave train. The shortest distance between the planes is equal to the wavelength (or multiples of it), and the slope of the planes determines the orientation of the wavenumber vector and the possible directions of wave propagation.

One should be aware that the path of the star through the atmosphere is generally not perpendicular to the local isopotential surface and it becomes more and more slanted (horizontal) as the star samples deeper atmospheric regions (Fig. 7). During the HIP 9369 occultation the horizontal velocity of the star image in the local topographic reference frame is about $V_h = 14.5$ km s^{-1}, whereas the vertical velocity just below the midoccultation level (where the peaks occur) is about $V_z = 1.2$ km s^{-1}. As a result the path of the star is very much horizontal and the observed vertical distance between peaks A, B, and C in the temperature profiles measured along the star path is much larger than the vertical distance between the corresponding planes. There is an approximate but straightforward geometrical relation between the observed vertical wavelength λ_{zo} (the vertical distance between the peaks) and the actual vertical wavelength λ_z (vertical distance between the corresponding planes) (Young et al., 1997):

$$|k_{zo}| = |k_z| \pm \left| \frac{\mathbf{V_h} \cdot \mathbf{k_h}}{V_z} \right| \pm \frac{\omega}{|V_z|}, \tag{12}$$

where $|k_z| = 2\pi/\lambda_z$ and $|k_h| = 2\pi/\lambda_h$ are respectively the magnitudes of the vertical and the horizontal wavenumber vectors, and ω is the frequency of the wave. The second term on the right-hand side of Eq. (12) reflects the slanted geometry of the planes and its sign depends on the exact observational setting (in our case it is a minus). The third term takes into account the motion of the phase planes of the wave and is positive (negative) for an upward (downward) propagation of the phase.

The type of an atmospheric wave is largely determined by its frequency. For a given set of wavenumbers (k_x, k_y, k_z) there are three different solutions for the wave frequency of the general wave equations, corresponding to three different propagating wave modes: an acoustic wave, an inertia-gravity wave, and a planetary wave. We shall consider the three different possibilities.

8.1. Inertia-gravity waves and planetary waves

The relevant dispersion equation for an inertia-gravity wave is

$$\omega^2 = f^2 + \frac{N^2 k_h^2}{k_z^2 + \dfrac{1}{4H^{*2}}}, \tag{13}$$

where $N = 0.018$ s^{-1} is the buoyancy frequency, $f = 3.363 \times 10^{-4}$ s^{-1} is the Coriolis parameter, and H^* the density scale height. For the wave to propagate vertically the frequency of the wave ω must be larger than f and smaller than N. This results in an upper limit for the last term in Eq. (12), yielding $(\omega/V_z) \ll 1.5 \times 10^{-5}$. For an observed vertical wavelength of about 10 km ($k_{z0} = 6.28 \times 10^{-4}$) the correction to the actual wavelength due to the phase motion is less then 2.4% and the measured distance between the planes corresponds exactly to the wavelength of the inertia-gravity wave.

The observed plane system defines a wave with a vertical wavelength $\lambda_z = 3.0 \pm 0.9$ km and horizontal wavelength $\lambda_h = 70 \pm 34$ km. Note that because of the very slanted path of the star image through the atmosphere, the distance between peaks B and C indicated on the temperature gradient profile (Fig. 10a) is much larger than the derived vertical wavelength λ_z. With the use of the dispersion relation in Eq. (13), we determine a wave period $\tau = 125 \pm {}^{86}_{72}$ min. The wave propagates at an angle of $2.5° \pm {}^{3.7}_{1.3}$ with respect to the vertical and at $82° \pm {}^{5.4}_{17}$ with respect to the zonal, east–west, direction. The vertical and the horizontal phase speeds of the wave are $0.4 \pm {}^{0.8}_{0.2}$ ms^{-1} and $9.33 \pm {}^{23}_{6.4}$ ms^{-1}, respectively. The large uncertainties in the horizontal parameters and in the wave period are a result of the poor time sampling of the Mégantic lightcurve. The observed wave is propagating very close to the local north–south direction. Because the occultation provides a single snapshot of the position of the wave, there is a 180-degree ambiguity in the direction of wave propagation. If, however, one makes the reasonable assumption that the wave is transporting energy upward from deeper atmospheric regions, then the wave phase planes should be moving downward. Using the geometry of the observed phase planes one can then determine the horizontal direction of phase propagation. From Fig. 14 it is clear that for the wave to transport energy upward, it should propagate from the north polar region toward the equator. In this exercise one should keep in mind that for internal gravity waves the wave group velocity, $\vec{C}_g$, is perpendicular to the wave phase velocity, $\vec{C}_p$. As a result the wave energy flux is perpendicular to the wavenumber vector and a downward propagating phase corresponds to an upward energy flux (Fig. 14, Case I).

Of course we cannot rule out the possibility of a downward propagating energy. This would be the case if the wave is generated at higher altitudes or if an upward propagating wave is reflected from higher atmospheric regions. In this case the wave phase would be propagating poleward (Fig. 14, Case II).

At this point there are two questions to be addressed: Is it possible to observe a wave with such a short horizontal wavelength with an occultation technique and is the presence of wave signatures consistent with a gravity wave propagation at the observed pressure level? Most of the refraction of the stellar light during an occultation occurs within a finite horizontal region $L = \sqrt{2\pi r H} \approx 3600$ km, where r is the planetary radius and H is the atmospheric scale height. As a consequence, occultations are not very sensitive to atmospheric structures with a large vertical-to-

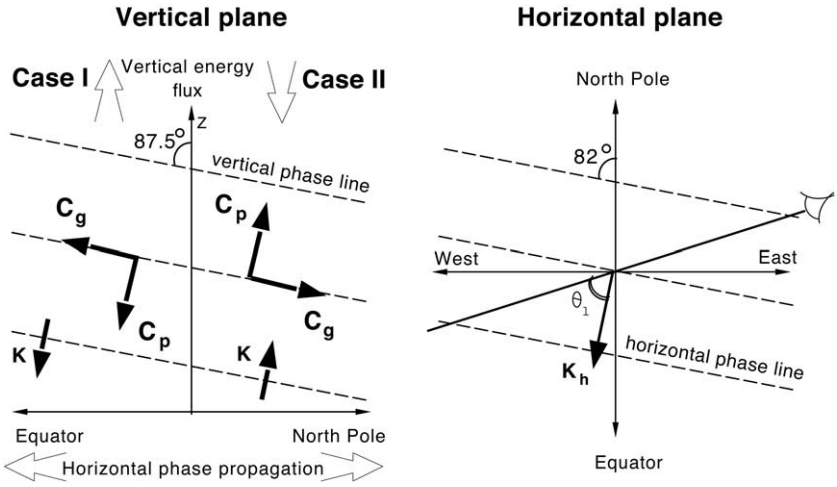

Fig. 14. Schematic representation of the observed gravity wave. The left and right panels show the wave geometry in a vertical plane and in a horizontal plane, respectively. The wave phase lines (vertical and horizontal) are plotted with dashed lines. The inclination of the phase lines is exaggerated for better viewing. The angles of inclination are indicated. The thick solid line in the right panel shows the line of sight during the occultation. Horizontally, the observed wave is propagating almost parallel to the planetary meridian. We illustrate the two possible cases (Case I and Case II in the left panel) for the direction of wave propagation (see text for discussion). The wave group and phase velocities, C_g and G_p, respectively, are shown as thick solid arrows along with the wavenumber vector, K.

horizontal (along the line of sight) aspect ratio. Sicardy et al. (1999) demonstrated that the amplitude of the stellar flux fluctuations which result from the presence of a monochromatic atmospheric gravity wave with a vertical wavelength λ_z and a projection of the horizontal wavelength along the line of sight $l = \lambda_h/\cos\theta_l$ is significantly reduced if

$$\frac{l}{\lambda_z} \leq \eta, \quad \eta = \sqrt{\frac{r}{4H}}, \tag{14}$$

where θ_l is the angle of the line of sight with respect to the horizontal direction of wave propagation. For Jupiter, $\eta \approx 25$ and therefore a wave with $\lambda_z = 3$ km and $\lambda_h = 70$ km should be well within the observable range since $l/\lambda_z = 119 \gg \eta$ (the angle between the local east–west direction and the line of sight is 3.34°).

To answer the second question we consider the dissipative effect of molecular viscosity, thermal conduction, and eddy diffusion on the propagation of inertia-gravity waves. For a detailed discussion and a full mathematical treatment of the problem we refer the reader to Matcheva and Strobel (1999). Here we shall focus only on the results. In a conservative atmosphere with no vertical wind shear the wave amplitude is increasing exponentially with altitude inversely proportional to the square root of the atmospheric density. At high altitudes (low density levels) the molecular viscosity becomes important for the wave motion and inhibits the amplitude growth. At the altitude where the wave reaches a maximum amplitude the dissipation exactly cancels the exponential growth of the wave. The corresponding value of the molecular viscosity at this altitude is (French and Gierasch, 1974)

$$\nu = \frac{1}{2H}\frac{\omega^2 - f^2}{\omega k_z^3}, \tag{15}$$

Above this altitude the wave amplitude is heavily damped and is completely obscured within a scale height. According to Eq. (15) a wave with the observed parameters reaches a maximum amplitude at an altitude where $\eta = 1.2$ m^{2}s^{-1}, about two scale heights below the region where the peaks occur (Fig. 15). The presence of atmospheric eddies will further increase the wave dissipation and will move the

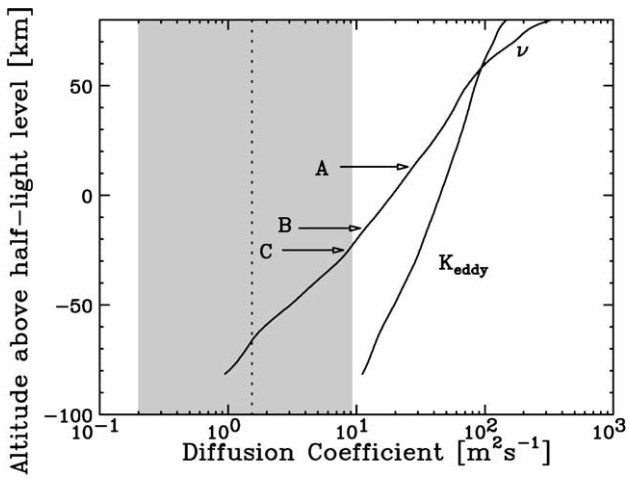

Fig. 15. Dissipation of inertia-gravity waves. The molecular viscosity ν and the eddy diffusion coefficient K_{eddy} are shown in the region of interest (after Atreya, 1986). The value of the diffusion coefficient for which a wave with the observed parameters is dissipated is plotted with a dotted line. The shaded region illustrates the uncertainty in the diffusion coefficient at the level of maximum amplitude. The locations of the observed peaks are indicated with arrows.

level of maximum amplitude to even lower altitudes. A wave with a larger vertical wavelength is needed in order to be able to interpret the observed layered system as an inertia-gravity wave.

For a planetary wave with the same set of wavenumbers (k_x, k_y, k_z) the wave frequency is even smaller than for the inertia-gravity wave. This means that a planetary wave with the same vertical and horizontal wavelengths will dissipate at lower altitude than the corresponding inertia-gravity wave. Therefore the observed layers are not signatures of a single planetary wave train propagating in the stratosphere.

8.2. Acoustic waves

Is it possible that we are detecting an acoustic wave? The dispersion relation for an acoustic wave is

$$\omega^2 = c_s^2 \, (k_h^2 + k_z^2), \tag{16}$$

where c_s is the speed of sound. The vertical and the horizontal phase speeds of an acoustic wave must be larger than c_s for the wave to propagate. At the altitude of interest the sound speed in the jovian atmosphere is about 1.1 km s^{-1} and is comparable to the velocity with which the star image moves through the atmosphere. A difficulty arises from the fact that, although the observations of the occultation event from the three observing stations are nearly simultaneous, there is a 4-minute time delay between the observations at Mégantic and Catalina. The time difference between Catalina and Kitt Peak is less significant (~3 s), but the derived three-dimensional geometry of the wave phase planes is not reliable anymore, since the assumption on the simultaneity of the observations is violated, at least when an acoustic wave is considered.

The only parameter that we have available now is the observed distance between the peaks A, B, and C along the star path, which corresponds to the observed vertical wavelength λ_{z0}. However, in the case of an acoustic wave, one should expect a very large difference between the observed and the actual wave parameters, because of the large phase speed. Therefore, the use of λ_{z0} as a representative value for the real vertical wavelength λ_z is not justified. Taking the Catalina ingress occultation as an example, we obtain from Eq. (12) that the actual wavelength of a vertically propagating acoustic wave ($k_h = 0$) would be about two times larger than the observed one if the wave was propagating upward and an order of magnitude smaller if the wave was propagating downward.

In general acoustic waves can propagate at very high altitudes in the atmosphere and they are a possible candidate for the observed signatures in the temperature profiles. However, additional constraints are needed to pinpoint the real wave parameters in order to estimate the energy of the waves and to determine the altitude where this energy is deposited.

9. Conclusion

The observation of the HIP 9369 occultation from four different locations on Earth has allowed us to obtain temperature profiles in the northern polar region and to estimate an increase of temperature between the equator, the mid-latitudes, and the high latitudes that is consistent with previous observations of Jupiter. We also demonstrate the superiority of the continuous wavelet transform for the scale–time analysis of both lightcurves and temperature profiles. The power spectrum of the fluctuations in the retrieved temperature profiles shows a characteristic slope of -3, consistent with previous observations of other planetary atmospheres. We are able to identify and reconstruct the three-dimensional geometry of a system of three nearly parallel layers of large density gradient, causing sharp peaks in the measured stellar flux. We investigate the possibility that the observed layers are signatures of atmospheric waves propagating at high altitudes. We conclude that an inertia-gravity wave with the observed parameters is not consistent with the level of dissipation at this altitude. An acoustic wave interpretation is possible although the exact parameters remain poorly constrained.

Acknowledgments

We thank the French Programme National de Planétologie (CNES/INSU) for support in data acquisition and reduction. KM acknowledges the support by the European Community through the Marie Curie Fellowship Program (Contract HPMF-CT-2000-01005). BS received a grant from the Institut Universitaire de France for the trip to Mount Mégantic. This work is based on observations collected at the European Southern Observatory, Paranal, Chile (ESO Program 66.C-0070). Wavelet software was provided by C. Torrence and G. Compo and is available at URL: http://paos.colorado.edu/research/wavelets/.

References

Atreya, S.K., 1986. Atmospheres and Ionospheres of the Outer Planets and Their Satellites. Springer-Verlag, Berlin/Heidelberg.

Baum, W.A., Code, A.D., 1953. A photometric observation of the occultation of σ Arietis by Jupiter. Astron. J. 58, 1208, 108–112.

Cadet, D., 1977. Energy dissipation within intermittent clear air turbulence patches. J. Atmos. Sci. 34, 137–142.

Combes, M., Lecacheux, J., Vapillon, L., 1971. First results of the occultation of β Sco by Jupiter. Astron. Astrophys. 15, 235–238.

Cuby, J.-G., Barucci, A., de Bergh, C., Emsellem, E., Moorwood, A.F., Petr, M., Pettini, M., Tresse, L., 2000. Scientific results with ISAAC at the VLT, in: Bergeron, J. (Ed.), Proc. SPIE Vol. 4005, Discoveries and Research Prospects Form 8- to 10-Meter Class Telescopes, SPIE, Philadelphia, pp. 212–223.

Drossart, P., Sicardy, B., Roques, F., Widemann, T., Gladstone, R., Waite, J.H., Vincent, M., 2000. The methane homopause of Jupiter seen from the IR spectroscopy of star HIP9369 during its occultation by Jupiter. Bull. Am. Astron. Soc. 32, 1209D (abstract).

Farge, M., 1992. Wavelet transforms and their application to turbulence. Ann. Rev. Fluid. Mech. 24, 395–457.

French, R.G., Gierasch, P.J., 1974. Waves in the jovian upper atmosphere. J. Atmos. Sci. 31, 1707–1712.

French, R.G., Elliot, J.L., Gierasch, P.J., 1978. Analysis of stellar occultation data: effects of photon noise and initial conditions. Icarus 33, 186–202.

French, R.G., Elliot, J.L., Sicardy, B., Nicholson, P., Matthews, K., 1982. The upper atmosphere of Uranus: a critical test of isotropic turbulence models. Icarus 51, 491–508.

Grodent, D., Waite Jr., J.H., Gérard, J.C., 2001. A self-consistent model of the jovian auroral thermal structure. J. Geoph. Res. 106, 12933–12952.

Hinson, D.P., Jenkins, J.M., 1995. Magellan radio occultation measurements of atmospheric waves on Venus. Icarus 114, 310–327.

Hinson, D.P., Mangalhaes, J.A., 1993. Inertio-gravity waves in the atmosphere of Neptune. Icarus 105, 142–161.

Hubbard, W.B., Nather, R.E., Evans, D.S., Tull, R.G., Wells, D.C., van Citters, G.W., Warner, B., Vanden Bout, P., 1972. The occultation of Beta Scorpii by Jupiter and Io. I. Jupiter. Icarus 77, 41–59.

Hubbard, W.B., Haemmerle, V., Porco, C.C., Rieke, G.H., Rieke, M.J., 1995. The occultation of SAO 78505 by Jupiter. Icarus 113, 103–109.

Koop, C.G., 1981. A preliminary investigation of the interation of internal gravity waves with a steady shearing motion. J. Fluid. Mech. 113, 347–386.

Koop, C.G., McGee, B., 1986. Measurements of internal gravity waves in a stratified shear flow. J. Fluid. Mech. 172, 453–480.

Matcheva, K.I., Strobel, D.F., 1999. Heating of Jupiter's thermosphere by dissipation of gravity waves due to molecular viscosity and heat conduction. Icarus 140, 328–340.

McEwan, A.D., 1983. The kinematics of stratified mixing through internal wave-breaking. J. Fluid. Mech. 128, 47–57.

Nadeau, D., Murphy, D.C., Doyon, R., Rowlands, N., 1994. The Montreal near-infrared camera. Pub. Astron. Soc. Pacific 106, 909–914.

Orton, G.S., Friedson, A.J., Caldwell, J., Hammel, H.B., Baines, K.H., Bergstrahl, J.T., Martin, T.Z., Malcolm, M.E., West, R.A., Golish, W.F., Griep, D.M., Kaminsky, C.D., Tokunaga, A.T., Baron, R., Shure, M., 1991. Thermal maps of Jupiter-Spatial organisation and time dependence of stratospheric temperatures, 1980–1990. Science 252, 537–542.

Perrier, V., Philipovitch, Th., Basdevant, C., 1995. Wavelet spectra compared to Fourier spectra. J. Math. Phys. 36 (3), 1506–1519.

Philbrick, C.R., Grossman, K.U., Henning, R., Lange, G., Krankowsky, D., Offerman, D., Scmidlin, F.J., vonZahn, U., 1983. Vertical density and temperature structure over northern Europe. J. Atmos. Sci. 2, 121–124.

Roques, F., Sicardy, B., French, R.G., Hubbard, W.B., Barucci, A., Bouchet, P., Brahic, A., Gehrels, J.A., Gehrels, T., Grenier, I., Lebertre, T., Lecacheux, J., Maillard, J.P., McLaren, R.A., Perrier, C., Vilas, F., Waterworth, M.D., 1994. Neptune's upper stratosphere, 1983–1990: ground-based stellar occultation observations III. Temperature profiles. Astron. Astrophys. 288, 985–1011.

Sato, T., Woodman, R.F., 1982. Fine altitude resolution observations of stratospheric turbulent layers by the Arecibo 430 Mhz radar. J. Atmos. Sci. 39, 2546–2552.

Seiff, A., Kirk, D.B., Knight, T.C.D., Mihalov, J.D., Blanchard, R.C., Young, R.E., Schubert, G., von Zahn, U., Lehmacher, G., Milos, F.S., Wang, J., 1996. Structure of the atmosphere of Jupiter: Galileo probe measurements. Science 272, 844–845.

Sicardy B., 23 colleagues, 1999. The structure of Titan's stratosphere from the 28 Sgr occultation. Icarus 142, 357–390.

Smith, S.A., Fritts, D.C., VanZandt, T.E., 1987. Evidence for a saturated spectrum of atmospheric gravity waves. J. Atmos. Sci. 44, 1404–1410.

Theon, J.S., Nordberg, W., Katchen, L.B., Horvath, J.J., 1967. Some observations on the thermal behavior of the mesosphere. J. Atm. Sci. 24, 428–438.

Torrence, C., Compo, G.P., 1998. A practical guide to wavelet analysis. Bull. Am. Meteorol. Soc. 79, 61–78.

Vapillon, L., Combes, M., Lecacheux, J., 1973. The β Scorpii occultation by Jupiter. II. The temperature and density profiles of the jovian upper atmosphere. Astron. Astroph. 29, 135–149.

von Zahn, U., Hunten, D.M., Lehmacher, G., 1998. Helium in Jupiter's atmosphere: results from the Galileo probe Helium Interferometer Experiment. J. Geoph. Res. 103, 22815–22829.

Wand, R.H., Rastogi, P.K., Watkins, B.J., Loriot, G.B., 1983. Fine Doppler resolution observations of thin turbulence structures in the tropo-stratosphere at Millstone Hill. J. Geophys. Res. 88, 3851–3857.

Wasserman, L., Veverka, J., 1973. On the reduction of occultation light curves. Icarus 20, 322–345.

Young, L.A., Yelle, R.V., Young, R., Seiff, A., Kirk, D.B., 1997. Gravity waves in Jupiter's thermosphere. Science 276, 108–110.